Direct comparison of off-axis holography and differential phase contrast for the mapping of electric fields in semiconductors by transmission electron microscopy

Benedikt Haas, Jean-Luc Rouviere, Victor Boureau, Remy Berthier, David Cooper

Version of Record: https://www.sciencedirect.com/science/article/pii/S0304399118301116
Manuscript_912cecd1a6e70a893d295d258a03e338

Direct comparison of off-axis holography and differential phase contrast for the mapping of electric fields in semiconductors by transmission electron microscopy.

Benedikt Haas and Jean-Luc Rouvière

Univ. Grenoble Alpes, CEA, INAC 38000 Grenoble, France

Victor Boureau, Remy Berthier and David Cooper

Univ. Grenoble Alpes, CEA, LETI 38000 Grenoble, France[a]

(Dated: November 30, 2018)

Abstract

To provide a direct comparison, off-axis holography and differential phase contrast have been performed using the same microscope on the same specimens for the measurement of active dopants and piezoelectric fields. The sensitivity and spatial resolution of the two techniques have been assessed through the study of a simple silicon p-n junction observed at different bias voltages applied in-situ. For an evaluation of limitations and artefacts of the methods in more complicated systems a silicon pMOS device and an InGaN/GaN superlattice with 2.2-nm $In_{0.15}Ga_{0.85}N$ quantum wells is investigated. We demonstrate the effects of dynamical scattering on the electric field measurements in the presence of local strain-induced sample tilts and its dependence on parameters like the convergence angle.

PACS numbers: 85.30.De

[a] david.cooper@cea.fr

I. INTRODUCTION

There is a need to measure the electrical properties arising from active dopants or from charged interfaces in semiconductor devices with nm-scale resolution. There are several transmission electron microscopy (TEM) based techniques that exist which can be used to solve this problem each with their strengths and weaknesses. Methods utilizing plane wave illumination to measure the phase shift of the electron wave are summarized as holography and can be used to measure the local electric potential [1–3]. Another approach is to determine the deflection of a convergent beam which corresponds to the gradient of the potential which is known as differential phase contrast (DPC) [4–6].

There are many different configurations of electron holography, the better known versions being off-axis electron holography and in-line holography. In this paper we focus only on off-axis electron holography, although it has been shown that in-line holography can also have unique benefits such as using a low electron dose, not requiring a reference wave and being compatible with large fields of view [7–9]. However, in-line holography has difficulties retrieving low frequency components which can be problematic for some applications. DPC is implemented here using a four segment detector, but we discuss how this technique could be improved by the use of pixelated electron detectors that can account for intensity redistributions within the direct beam disc and are therefore in many cases advantageous [10–12]. In this paper we introduce each technique, discuss quantification and key points regarding the spatial resolution, sensitivity and the effects of dynamical diffraction. We then show results for the two techniques applied to a highly-doped p-n junction under applied bias to illustrate their capabilities when used to characterise this simple example of a specimen containing an electric field. We will then apply the two techniques to a doped CMOS device to benchmark their performance for 2D potential mapping. Finally, we will measure the piezo-electric field across a 2.2-nm-thick InGaN/GaN quantum well superlattice. For this measurement, a high field of several MVcm^{-1} is expected at the InGaN/GaN interface, but excellent spatial resolution is also required.

Unless otherwise stated, we have applied the techniques in their most simple form using standard lens configurations. For off-axis electron holography the experiments have been applied using a FEI Themis equipped with a Lorentz lens, a single electron biprism and a standard Gatan Ultrascan CCD detector. The DPC experiments have also been performed

using an aberration corrected FEI Themis equipped with a segmented semiconducting annular detector.

II. OFF-AXIS ELECTRON HOLOGRAPHY

Off-axis electron holography (now referred to as electron holography) uses an electron biprism to interfere an electron wave that has passed through a region of interest with a wave that has passed through a vacuum reference. This forms an interference pattern which is also known as a hologram. From the electron hologram, the phase, $\phi(\mathbf{r})$ of the electron wave can be recovered which can be directly linked to the projected electrostatic and vector potentials in and around the specimen using the relationship;

$$\phi(\mathbf{r}) = \frac{e}{\hbar v}\int_{-\infty}^{+\infty} V(\mathbf{r})\, dz - \frac{e}{\hbar}\int_{-\infty}^{+\infty} \mathbf{A}(\mathbf{r})\, dz, \tag{1}$$

where dz is the propagation direction of the beam, $\mathbf{r}$ is a position vector perpendicular to it, $V(\mathbf{r})$ is the electrostatic potential, $\mathbf{A}(\mathbf{r})$ the magnetic vector potential, v is the relativistic electron velocity and e is the elementary charge [2]. The first term describes the electrostatic part of the phase shift, while the second term is due to magnetic interaction. The electrostatic phase shift is proportional to the (projected) electrostatic potential in beam direction and the magnetic phase shift is proportional to the (projected) component of the vector potential in beam direction. Although electron holography is typically used for measuring the potentials in and around specimens , the electric field can also be obtained by,

$$\mathbf{E}(\mathbf{r}) = -\nabla V(\mathbf{r}). \tag{2}$$

Similarly the magnetic field can be calculated using

$$\mathbf{B}(\mathbf{r}) = -\nabla \times \mathbf{A}(\mathbf{r}). \tag{3}$$

When using holography for dopant profiling, we assume that the specimen is both non-magnetic and has been tilted to a weakly diffracting orientation. The local electrostatic potential can be quantitatively measured directly from the phase ϕ using the following formula,

$$\phi = C_E V t \tag{4}$$

where V is the electrostatic potential and t is the specimen thickness. The interaction constant, C_E is 1.01 $\times 10^7$ $V^{-1}m^{-1}$ for 80 kV electrons and 7.29 $\times 10^6$ $V^{-1}m^{-1}$ for 200 kV electrons. The measured phase is sensitive to two components of the electrostatic potential, the mean inner potential (MIP) which is the volume averaged electrostatic potential [13–15], V_0 and the dopant related potential, V_{dop}. The MIP can be measured directly by electron holography, and values that have been measured experimentally for the specimens examined in this work are 11.9 V for Si and 15.4 V for GaN [16, 17]. The important consequence is that the values of MIP that are present in most semiconductors are much higher than the changes in potential that are expected from active dopants. Thus, only small changes in specimen thickness will contribute strongly to the measured phase. Fortunately, these problems can be minimised by using focused ion beam (FIB) milling, where if sufficient care is taken both flat and parallel-sided specimens can be prepared. In addition, here we make the assumption that the field is contained within the specimen which can be the case for FIB prepared semiconductors where the damaged Ga implanted surface layers act as an isopotential [18]. However, this assumption is not always true, especially in the case of specimens that are electrically biased in the microscope [19].

Figure 1(a) shows a schematic of the setup for off-axis electron holography. A coherent source of electrons is required, then by applying a voltage to the electron biprism a reference electron wave that has passed through vacuum and electron wave that has passed through the specimen are overlapped to form the interference pattern. By increasing the voltage, the virtual electron sources, $S1$ and $S2$ move further apart to form a larger overlap of the waves which provides a wider interference pattern with finer fringes. Often the electron beam is made astigmatic in the perpendicular direction to the biprism as the spatial coherence increases when decreasing the angular spread of the electrons. Figure 1(b) shows an image of the electron biprism with no applied voltage. The dark line is the electron biprism and Fresnel diffraction can be observed on either side. Figure 1(c)-(g) then show that by increasing the biprism voltage, the fringes become finer and more numerous and the width of the interference pattern increases.

Figure 2 shows a schematic diagram of the hologram reconstruction process. Here an electron hologram has been acquired which contains a pMOS transistor device. The infor-

mation about the electron phase is contained in the interference fringes which are observed more clearly in the inset. To remove the distortions in the imaging system, a reference hologram which contains a vacuum region with no fields present is also required.

To obtain the phase information carried by the hologram, a Fourier transform is applied and a sideband is selected and moved to the origin of Fourier space. A typical radius for the mask for a strongly scattering object is either 1/2 or 1/3 of the carrier fringe frequency which limits the spatial resolution in the reconstructed phase and amplitude images [2, 3]. This is due to the presence of the conventional intensity image which is simultaneously recorded with the hologram. Therefore the spatial resolution in a reconstructed phase image is usually between twice and three times the fringe spacing. An inverse Fourier transform of the sideband is then applied which generates a complex image. The amplitude and phase information can be obtained by using equations 5 and 6, where A is the amplitude, ϕ the phase, $\Im$ the imaginary component of the complex reconstructed image and $\Re$ the real component.

$$A(x,y) = \sqrt{(\Re^2 + \Im^2)}, \tag{5}$$

$$\phi(x,y) = arctan(\Im/\Re). \tag{6}$$

The reconstructed phase image of the pMOS device is shown in Figure 2. Due to the changes in electrostatic potential from the active dopants, the n-type source and drain appears brighter than the p-type substrate region. As the dopant concentration is much less than 1 %, almost no amplitude contrast results between the doped and pure Si region.

The spatial resolution of an electron hologram reconstruction is determined by the size of the mask that is used in Fourier space to select the sideband. Therefore fine fringe spacings are required to achieve the best spatial resolution. The limited coherence of the electron beam will limit the width of the hologram and fringe spacing before the contrast begins to deteriorate. In addition, the need to record the hologram using a CCD camera means that for a given field of view, there are a finite number of pixels that can be used for recording and it is good practice to use at least 6 pixels to prevent information loss from sampling and from the MTF of the camera. A typical hologram acquisition setup would be to use a 2048 x 2048 pixel detector to record a hologram across a field of view of 500 nm with fringe

spacings in the range 1.5 to 2.0 nm such that each fringe is sampled by 6 - 8 pixels. These settings would provide phase images with spatial resolution in the range 3 - 6 nm depending on the reconstruction procedure used. In addition there are more advanced methods of reconstruction which can be used to suppress the sideband and increase the size of the mask used in Fourier space [22].

The phase sensitivity of a reconstructed phase image is given by the relationship;

$$\Delta\phi = \frac{\sqrt{2}}{\mu\sqrt{N}}, \tag{7}$$

where μ is the hologram contrast and N is the number of electron counts per pixel in the reconstructed phase image [20, 21]. It is important to optimise the contrast of the fringes against the hologram acquisition time (instabilities), fringe spacing (sampling) and the FEG operating conditions (intensity versus coherence) [23] that is used. The stability of modern electron microscopes allow electron holograms to be recorded for times in the range of 10 - 100 s in order to increase N before instabilities lead to a deterioration of the contrast [24]. An alternative is to acquire a large series of holograms and add them together [25]. By adding together a large series of holograms, phase sensitivities of more than $2\pi/1000$ have been reached [26, 27].

III. DIFFERENTIAL PHASE CONTRAST

Differential phase contrast is a STEM based technique where a focused electron beam is scanned across a region of interest and the deflection is measured by means of the intensity difference of the detector segments. This method which was proposed by Harald Rose [28, 29] and demonstrated by Dekkers in 1974 [30] has until now been used principally for the measurement of magnetic fields [4, 5, 31]. DPC has recently gained attention, partly due to improvements in hardware such as the use of circular scintillator / photomultiplier tube detectors in circular rather than annular geometries [32]. In addition to this, certain microscope companies have begun to introduce these detectors as standard. In this new wave of DPC research, there has been a focus on mapping at atomic resolution [33–36] as well as the measurement of electrostatic potentials [37–39]. In this section we assume that the principle action of the electric field is to induce a shift of the diffraction disk without considering intensity redistribution within it. This holds for a homogeneous electric field

that produces only a one-dimensional phase ramp (as it is the case for a plate capacitor). Therefore, in this section we focus on what is known as the "disk shift" method for the quantitative measurements of fields using an annular detector.

The influence of electric and magnetic fields on the beam can be explained in a semi-classical model, where no scattering or energy loss of the beam is assumed as for a beam deflected by a field in vacuum [40]. For the case of an electric field, the force acting perpendicularly on the electron beam is proportional to the field component perpendicular to the beam projected in beam direction and the electron charge,

$$\mathbf{F}_\perp(\mathbf{r}) = -e\,\mathbf{E}_\perp(\mathbf{r}). \tag{8}$$

From Newton's second law of motion this force $\mathbf{F}_\perp(\mathbf{r})$ can also be expressed in terms of an acceleration perpendicular to the beam direction $\mathbf{a}_\perp(\mathbf{r})$ and the relativistic mass of the electron m_e^* as,

$$\mathbf{F}_\perp(\mathbf{r}) = \mathbf{a}_\perp(\mathbf{r})\,m_e^*. \tag{9}$$

The beam needs a time τ to traverse the field containing region of distance (here the sample thickness), t , which is given by the initial electron velocity v_0 as,

$$\tau = \frac{t}{v_0}. \tag{10}$$

Because the beam is only sensitive to the perpendicular field component projected along the beam direction over t, solely the average field strength can be determined. While traversing through a region containing a field t, the electron picks up a velocity component $v_\perp$ perpendicular to v_0 that can be expressed as,

$$v_\perp = -\frac{E_\perp\,e\,t}{m_e^*\,v_0}. \tag{11}$$

The deflection angle, γ can be described in terms of the velocities as,

$$\gamma = arctan(\frac{v_\perp}{v_0}) \approx \frac{v_\perp}{v_0}. \tag{12}$$

The last expression corresponds to the small angle approximation which is valid for the deflections of significantly less than 1 mrad that is observed for the typical field strengths

(< 5 MVcm^{-2}) , sample thicknesses ($<$ 200nm) and electron energies (80-300 kV) that are used. Therefore, the magnitude of the electric field component perpendicular to the beam can be expressed as,

$$E_{\perp} = -\frac{\gamma\, m_e^*\, v_0^2}{e\, t}. \tag{13}$$

For a given beam energy all the parameters are known, except for t and γ (the beam deflection). For an operating voltage of 200 kV, Equation 13 simplifies to

$$E_{\perp} = -\frac{\gamma}{t} \cdot 3.438 \cdot 10^5 V. \tag{14}$$

An expression for the B-field can also be derived in a similar manner. However, as this paper discusses the measurement of electric fields, the derivation is omitted and can be found elsewhere [40].

$$B_{\perp} = \frac{\gamma\, m_e^*\, v_0}{q\, t}. \tag{15}$$

Again for an operating voltage of 200 kV, Equation 15 simplifies to;

$$B_{\perp} = -\frac{\gamma}{t} \cdot 1.649 \cdot 10^{-3}. \tag{16}$$

Thus the beam deflection is antiparallel to an electric field and perpendicular to a magnetic field.

Figure 3 shows a schematic of the experimental technique using the example of a doped pMOS device. An electron beam of a total diameter of twice the inner diameter of the segmented annular detector is carefully positioned such that the four segments are evenly illuminated. This setup is similar to the one from Shibata et al. [6], which showed good robustness and linearity. However, other setups where the beam convergence rather matches the inner detector angle for increased sensitivity have been used e.g. by Lohr et al. [37]. In a well aligned microscope as the beam is scanned across the dashed line indicated in 3(f), we find that in position A, in the n-doped region with no internal electric field the intensities in the different outputs should in principle remain constant as shown in Figure 3(a). As the beam traverses the depletion region indicated B between the p-doped source and the n-doped gate then γ can be measured by comparing the intensities in the different segments as shown in Figure 3(b). As the beam continues to the p-doped source region C -

which does not contain a field - the beam returns to its original position in the diffraction plane again shown in Figure 3(c). Figure 3(d) shows the different intensities measured in scanned images of a pMOS device and (e) demonstrates that by subtracting the intensities in opposite segments and correcting for the mis-orientation of the detector segments relative to the specimen, the electric field can be directly obtained by using a simple calibration procedure. Diffuse scattering (that increases with sample thickness) poses a problem for the segmented detector setup, because intensity is redistributed in the diffraction plane. As this scattering exhibits normally rotational symmetry the effect is to overall reduce the measured DPC signal by increasing the amount of electrons that impinge on all segments. The chosen setup here, where the semi-convergence angle is twice the inner detector radius leads to a large portion of the beam (75%) hitting the detector and thus to a certain reduction of the effect of diffuse scattering. For thin samples the effect is generally negligible, but for thicker samples it can have an effect [33].

DPC experiments from literature can be grouped into roughly three different families of settings, which we refer to as high-resolution (HR), nano-beam (NB) and low-magnification (LM). Typical values for experimental parameters of these three modes can be found in Table I. The HR-DPC mode uses a large convergence angle of around 20 mrad which results in probe sizes below 0.1 nm (for the case of spherical aberration correction of the condenser system). To have a suitable beam size in the diffraction plane (here a beam with a diameter of twice the inner detector angle) the camera length needs to be adjusted. For the HR-DPC setting this results in a typical camera length of around 0.1 m (which is linked to the physical size of the detector). This short camera length means that the magnification of beam deflections, and thus the sensitivity, is rather low. A similar setup has been used to reveal the electric field of individual atomic columns [36]. The second mode is NB-DPC. Here, to achieve better sensitivity, the camera length is increased to around 1 m. However to maintain the size of the beam relative to the detector, the convergence angle is reduced to around 2 mrad and thus the resulting (diffraction limited) probe size is around 1 nm. This is illustrated in Figure 4(a-f) showing schematics of the optical setups of the beam relative to the detector. Reducing the convergence angle to match the beam to the detector has important consequences. Figure 4(g) shows a plot of the probe size of a diffraction limited imaging system as a function of the convergence angle showing that the choice of camera length (sensitivity) affects directly the spatial resolution. This NB-DPC mode is useful

for piezo-electric structures, such as hetero-epitaxial quantum wells, where the strength of the electric fields is significantly lower than for atomic fields, but a 1 nm or better spatial resolution is still required. An example of NB-DPC is the investigation of the fields in InGaN/GaN structures [39]. In the case of LM-DPC, a low-magnification mode is used, in which the objective lens is (almost) switched off. Here the camera length is increased by one order of magnitude to around 10 m, which leads to a high magnification of the beam deflection and thus a high sensitivity. With this mode even the rather weak electric fields at the depletion region of GaAs p-n junctions have been observed [6]. However, very small convergence angles of the scanning probe on the order of 0.2 mrad are used here, resulting in probe sizes of roughly 10 nm.

An additional consideration when adjusting the camera lengths and convergence angles is the adjustment of the descan alignment which is used to prevent the transmitted beam from moving as it is scanned across the specimen using the STEM coils. This movement of the beam on the detectors will introduce a gradient on the field map. In HR-DPC mode, this alignment is relatively straightforward at low camera lengths and residual gradients on the signal can be corrected. However, in NB-DPC mode, it is difficult to make fine enough descan and pivot point alignments for camera lengths of more than 1 m. This means that only high magnifications can be used, otherwise the large shifts of the transmitted beam during scanning lead to a non-linear intensity signal as well as saturation of the detector which cannot be corrected for. In LM-DPC mode, again it is relatively easy to correct the descan for the relevant camera lengths.

IV. QUANTIFICATION OF DPC

Although DPC is not directly quantitative, there are several methods that can be used to provide a value of the fields. One calibration method is to use a plate capacitor mounted onto a specimen holder to measure the beam deflection for a known applied field. Although this method is straightforward in principal, a dedicated specimen holder is required and great care has to be taken to ensure that the capacitor geometry applies the intended field [38]. Another calibration method is to compare results that have been acquired by electron holography on a simple specimen which is easy to measure, such as a silicon p-n junction.

An additional calibration method is presented here where the beam relative to the de-

tector is intentionally shifted using the diffraction shift coils. DPC images are acquired in vacuum before and after the displacement and the positions of the diffraction disc are recorded on a camera. The intensity difference can be related to the imposed beam shifts that can be obtained from cross-correlating the recorded camera images. For a calibrated camera length and pixel size the shift of the beam in pixels directly yield the deflection angles. The result of such an experiment is given in Fig. 5. Here the imposed beam shift vector is compared to the DPC intensity difference vector for several different beam positions that were measured using the camera. The intensity of the individual segments is normalised by dividing them by the sum of all segments. For each position, the intensity difference of diagonal segments, e.g. between segments A and C as ΔI_{AC}, is determined and the value of the centre position $\Delta I_{AC,0}$ is subtracted. The rotation between the detector segments and the camera plane can be calculated using the shifts in the two camera axes relative to the centre position $shift_x$ and $shift_y$

$$\omega = arctan\left[\frac{(\Delta I_{AC} - \Delta I_{AC,0}) \cdot shift_y - (\Delta I_{BD} - \Delta I_{BD,0}) \cdot shift_x}{(\Delta I_{AC} - \Delta I_{AC,0}) \cdot shift_x - (\Delta I_{BD} - \Delta I_{BD,0}) \cdot shift_y}\right]. \tag{17}$$

Afterwards, the intensity differences can be calculated in the detector coordinate system as

$$\begin{pmatrix} \Delta I_x \\ \Delta I_y \end{pmatrix} = \begin{pmatrix} cos(-\omega) & -sin(-\omega) \\ sin(-\omega) & cos(-\omega) \end{pmatrix} \begin{pmatrix} \Delta I_{AC} \\ \Delta I_{BD} \end{pmatrix}.$$

Once the convergence angle has been measured, the disc size on the camera directly yields the absolute deflection angle. Knowing the deflection angle from the intensity change of the DPC allows a calibration of the electric field by using Equation 14 once the sample thickness has been measured. For a given set of parameters (camera length, convergence angle, detector contrast/brightness settings) the intensity difference is then calibrated relative to the beam shift.

For the case of a real (thick) samples, the overall intensity is reduced to scattering and absorption leading to a reduction of intensity. This is accounted for by using the normalized intensity differences. For rather homogeneous samples like FIB lamellas of a Si diode it suffices to normalize all intensities to the reduced intensity measured at one point but especially for inhomogeneous samples (changing chemistry or thickness) it can be accounted

for by dividing the intensity difference image point by point by the image obtained from summing the images of all segments.

V. DIFFRACTION, SPECIMEN PREPARATION AND KNOWN ARTEFACTS

There are many papers that study artefacts that can be present in electron holography data of thinned semiconductor specimens [41–44]. One artefact that has been well studied is known as the inactive thickness which is due to both charging of the specimen surfaces [45–47] and from damage resulting from FIB milling [49] which leads to a layer of inactive dopants on each surface of the specimen. The inactive thickness is a sub-surface crystalline layer in the specimen and its presence leads to a reduction of the built in potential V_{dop} compared to the expected value for a perfect bulk-like situation. The inactive thickness is strongly dependent on the dopant concentration in the specimen and can be as low as 20 nm for highly doped specimens that are prepared using low energy Ga ions to many hundreds of nm for weakly doped specimens [48]. A consequence of this is that the very thin specimens that are typically considered very suitable for TEM are unsuitable for the measurement of dopants. As such, thicker specimens in the range 200 - 500 nm are required which leads to problems with projection effects and dynamical diffraction. A positive aspect of the damaged surface layers in FIB-prepared doped semiconductors is that the amorphous surface layer acts as an equipotential which can suppress the fringing fields in vacuum and as such simplify the quantification of the measured phases.

The key to obtaining interpretable potential maps of the specimens in the TEM is to limit the effect of dynamical diffraction [18]. Specimens cannot be observed on a zone axis as dynamical diffraction will dominate the image and the strong phase changes of the electrons will destroy the interference patterns. Even away from the zone axis, the presence of dynamical effects can lead to a phase map that is not interpretable. Therefore the specimen is typically tilted along a crystallographic axis whilst preserving the projection of the measured potential and fine specimen tilts are used until the region of interest becomes "bright" in bright field mode. Typically the specimen is tilted from 1 - 5 degrees from a zone axis which can have important consequences when examining the latest generation of CMOS-type semiconductor devices whose dimensions can be less than 10 nm.

Although there are many papers that discuss the use of electron holography to measure

the fields in piezoelectric materials [50, 51], no systematic study of the artefacts has been performed. Publications exist which suggest these specimens should not be prepared by FIB milling [52] and that only polishing and low energy Ar milling should be used. In this work, we have used careful FIB milling at low operating voltages.

There are few publications that discuss the artefacts that are present when using DPC for the measurement of electrostatic fields [53]. However, it is reasonable to assume that all of the artefacts that are present in holography are also relevant here. In order to demonstrate the problems of dynamical diffraction that are present when examining thick specimens using a convergent beam, JEMS simulations have been performed [54]. Figure 6 shows simulated Convergent Beam Electron Diffraction (CBED) patterns for a 200 kV electron beam with a convergence angle of 100 mrad incident on (a) 100 nm thick GaN specimen and (b) a 300 nm thick silicon specimen tilted 1.5 degrees from a zone axis which is a typical specimen orientation that is used for field mapping. The GaN specimen is near the $[11\bar{2}0]$ zone axis and the silicon specimen the $[1\bar{1}0]$ zone axis. It is clear that for the 100 nm thick GaN specimen there are many features in the CBED pattern compared to the 300 nm thick CBED pattern from the silicon specimen. The circles in the CBED patterns represent a 4 mrad convergence angle suggesting that for the GaN specimen, it would be more difficult to find an orientation with homogenous disk intensity occurring. For the much thicker silicon specimen, there are larger areas of homogenous contrast and as such it is much more straightforward to perform fine tilts so that that the dynamical diffraction contrast can be minimised across the field of view.

All of the specimens examined here were prepared using an FEI Strata 400. FIB milling was used as it allows a specimen to be prepared from the region of interest with nm-scale site specificity. Importantly, the TEM lamella should be flat with parallel-sides as the measurements of both the potentials and fields are strongly dependent on the specimen thickness. For the doped silicon p-n junctions and pMOS devices, thick specimens in the range 220 to 240 nm were prepared. An operating voltage of 30 kV was used for the rough milling to a total specimen thickness of 3 microns which were then finished at 8 kV as this provides a compromise between the reduction of specimen damage whilst maintaining the parallel sides that are required for holography. For the GaN/InGaN multilayer specimens with small quantum wells it is mandatory to obtain thickness of below 100 nm to be able to tilt into weakly diffracting orientations without losing the features in projection. Here

16 kV ions were used to maintain the parallel sides to a final specimen thickness of 100 nm with an additional short 2 kV cleaning to minimise the thickness of the amorphous layers.

VI. FIELD MAPPING OF A SILICON P-N JUNCTION

As a first test, a symmetrically doped p-n junction specimen with a dopant concentration of 1x10^{19} cm^{-3} has been examined [48, 55]. As the specimen is grown using epitaxy, the junction is not abrupt, however by combining SIMS measurements and by using textbook equations, a V_{dop} of 1.06 V leading to a field of 0.21 MVcm^{-1} is expected in the p-n junction [56]. The TEM grid holding the specimen was connected to a chip which was then mounted into a Nanofactory piezo contact holder and reverse biased such that the approximate sensitivity of the different techniques could be assessed as a function of the applied voltage. Before FIB preparation, the top surface of the specimen was cleaned using HF vapour treatment and the top surface sputter coated in gold to provide a good electrical contact with the tungsten piezo controlled probe. A crystalline specimen thickness of 225 $\pm$ 5 nm was measured by CBED. Figure 7(a) shows a STEM image of the diode that was examined and (b) shows the current / voltage response suggesting that the specimen still behaves as a diode due to the careful specimen preparation and contacting. Electron holograms and DPC STEM images were acquired during the same TEM session with the p-n junction at different bias voltages. To illustrate the effects of applying a reverse bias voltage, Figure 7(c) shows a holography phase image, demonstrating the strong contrast that is present across the differently doped regions at a reverse bias of 4 V. Figure 7(d) shows the calculated potential that was obtained from the measured phase across the indicated region in (c) as the reverse bias is increased.

Figure 8(a) shows the beam deflection measured from the electric field, E_z, in the [001] direction perpendicular to the junction at zero bias voltage and (b) at 4 V reverse bias acquired using a typical HR-DPC beam setting of 21 mrads beam convergence angle, a camera length of 0.115 m and an acquisition time of 80 s for a 1024x1024 pixel image. The convergence angle was set such that the diameter of the beam was twice the inner diameter of the segmented detector. Here the signal has not been quantified and the units are from the difference in detected intensities in the segments of the detector. The electrical junction cannot be observed by the naked eye at zero reverse bias due to the low sensitivity of the

HR-DPC but becomes clearer once a reverse bias voltage is applied. Figure 8(c) shows profiles extracted across the maps which have been averaged across 1.6 μm. When using LM-DPC mode with a camera length of 12 m and a convergence angle of 0.2 mrads the junction is clearly visible at both 8(d) zero bias and (e) 4 V reverse bias. Figure 8(f) shows profiles acquired across the field map with a sampling of 2.86 nm/px and averaged over 200 nm. The resolution (probe size) of this LM-DPC data is 7.5 nm.

Electron holograms were also acquired. Here the goal was to maximise the field of view which led to the need to use a low biprism voltage so that the fringes could be adequately sampled by the CCD camera. As such, coarse holographic fringes of 2.5 nm were used with an overall holographic width of 600 nm and an overall field of view of 1200 nm for an acquisition time of 8 seconds. In order to perform this experiment using the Nanofactory specimen holder, it was necessary to rotate the biprism 180° from it's "stable" position. The electron biprisms in our two FEI Titan microscopes are more stable when they are fully rotated to an endstop position. Thus the electron holograms were acquired with only 10 % contrast instead of the normal 20 - 30 % leading to a signal to noise ratio that would be much less than usual. The holograms were reconstructed to provide a spatial resolution of 7.5 nm in the potential maps. The potential maps obtained by off-axis electron holography are shown in 8(g) and (h) and the quantitative measurement of the fields calculated using Equation 2 are shown in (i). The sampling of the profile is 3.04 nm/px (from binning the original sampling by 8) and it was averaged over 200 nm (same as the LM-DPC profile). The quantitative measurement of the electric field by electron holography is 0.175 ± 0.02 MVcm^{-1} which is less than expected from theory due to the presence of the inactive thickness.

From these results it is possible to obtain a feeling for the signal to noise and spatial resolution of the different techniques which also appear in the Table II. Here the signal to noise was assessed from measuring the Root Mean Squared (RMS) noise in a single profile averaged across 200 nm. The pixel size for HR-DPC is 3.42 nm, LM-DPC 2.86 nm and for holography (from binning by 8) 3.04 nm, while the resolution for HR-DPC (probe size) is below 0.1 nm, LM-DPC 7.5 nm and for holography (from the reconstruction) also 7.5 nm. Clearly, the HR-DPC set-up does not provide an adequate sensitivity to measure the low values of fields that are expected in doped specimens. The LM-DPC set-up provides a signal to noise of 45 for the field measurement, but at the expense of spatial resolution. An increase in camera length from HR-DPC to LM-DPC of around 100 times is the reason for the 75

times higher signal-to-noise ratio. The performance of the holography for the settings used is roughly equivalent to the LM-DPC results when the electric field profiles are compared. However for the measurement of electrostatic potential, the signal to noise of holography is 470 compared to the value of 55 for the electric field. The reduced signal to noise ratio for the field results from increased noise caused by numerically calculating the derivative of the data. These figures provide only approximate assessment of the capabilities of the techniques used in their most standard conditions, for fields of view of around 1 micron. Of course the signal to noise in all of these experiments could be improved by using data averaging techniques or more appropriate microscope settings, such as better sampling of the holographic fringes on the CCD at expense of field of view for holography. For DPC it is also possible to integrate the signal to provide measurements of the electrostatic potential using the so called iDPC method, this approach is known to improve the sensitivity for atomically resolved imaging [57] and more experimental work is required to assess the possible improvements for medium resolution imaging of semiconductor specimens.

VII. ACTIVE DOPANT PROFILING IN SILICON CMOS DEVICES

There are many papers that discuss the use of electron holography to measure the potentials in silicon CMOS devices [58–69], however there are no published results that have been obtained using DPC. To test the two techniques on a real specimen which was at the same time not too challenging, an older generation 90-nm-gate-width p-MOS device was examined [70]. Here a step in potential of ~ 0.9 V is expected across a distance of 20 nm which leads to an expected electric field of 0.45 MVcm^{-1}. The interest in studying this device is that due to its finite size it is not possible to average the measured signal across a wide area. In addition, the presence of features such as the salicided metal contacts, the high-k metal gate and the physical gate structure will introduce mechanical strain into the specimen which will make it much more difficult to find the optimum orientation to reduce the dynamical diffraction contrast. The specimen thickness was measured to be 250 ± 5 nm by CBED. Figure 9(a) shows a HAADF STEM image of the device. Electron holograms were acquired using a standard Lorentz lens configuration with a field of view of 360 nm and a biprism voltage of 242 V was used to provide interference fringes of 2.0 nm. By taking advantage of the excellent mechanical and electrical stability of the electron microscope and with the

biprism in the "stable" position, the hologram was acquired for 64 seconds without affecting the recorded fringe contrast. Figure 9(b) shows a potential map that has been calculated from the reconstructed phase image and the p-type source and drain and n-doped gate can be clearly differentiated. Figures 9(c) and (d) show E_z and E_x respectively. The equivalent field maps acquired by LM-DPC are shown in Figure 9(e) and (f). Here a camera length of 12 m and a convergence angle of 200 μrads was used to provide a spatial resolution of 7.5 nm. LM-DPC field maps with a size of 1024^2 pixels was acquired for 80 seconds. The maps have been Fourier filtered to reduce the scan noise. The 1024^2 pixel field maps shown in Figure 9(g) and (h) were acquired in HR-DPC mode using a camera length of 115 mm, a convergence angle of 21 mrads and an acquisition time of 80 s. Using these settings, the electric field cannot be measured.

The quantitative measurements of both the potential and E_x measured by electron holography and DPC are shown in Figures 10(a) and (b) respectively. Profiles have been extracted from across the gate region that is indicated in 9(a). The holography profile has been averaged across 5 nm which corresponds to the approximate spatial resolution in the reconstructed phase image. The potential has been measured as 0.78 ± 0.05 V which is less than is expected from theory and can be explained from specimen preparation artefacts. As E_x has been calculated from the experimental potential profile in (a), it is very sensitive to experimental noise due to the differentiation term shown in Equation 11. The DPC field profile extracted from Figure 9(c) has also been averaged across 5 nm. The quantification has been performed by calibrating the intensity of the detected signals on the segments compared to the signals that were measured in Figure 8 by electron holography. Here, a value of 0.17 $MVcm^{-1}$ that was measured across the p-n junction by electron holography corresponds to a measured DPC signal (intensity difference signal divided by total intensity on all segments) of 4.33 ± 0.06 %. This comparative quantification is approximate due to problems with precisely centering the beam, limiting beam drift between measurements and the alignment of descan for long camera lengths in HR STEM modes. Here a peak-to-peak measurement of E_x can be made, which is 0.35 ± 0.1 $MVcm^{-1}$ measured by electron holography and 0.3 ± 0.02 $MVcm^{-1}$ by DPC. Again, both of these values are less than expected from theory.

Here we have shown that both LM-DPC and electron holography can be used to measure the fields in relatively large silicon CMOS devices which typically have step in potentials of around 1 V and internal fields in the range 0.1 - 1.0 $MVcm^{-1}$. The experimental problems

for the two techniques are the same in that thick specimens need to be prepared to limit the effects of the inactive thickness and for both techniques the key is to tilt the specimen to a weakly diffracting condition such that contributions from dynamical diffraction do not contribute significantly to the measured signals.

Clearly electron holography is adapted for the measurement of potentials rather than electric fields. It is possible to further improve the spatial resolution by using finer holographic fringes whilst simultaneously reducing the overall hologram width and thus using a smaller field of view, the signal to noise can be maintained or increased by adding stacks of holograms together. For the LM-DPC the spatial resolution cannot easily be improved as the convergence angle that is required such that the beam is incident on the fixed size detector is in the range 100 - 200 μrad. Of course this could be improved by using larger segmented detectors (or pixellated detectors). However, intermediate camera lengths in the range 1 - 3 m leading to convergence angles of 2 - 4 mrad combined with the use of data averaging would provide a better compromise between spatial resolution and signal to noise.

VIII. HIGH RESOLUTION FIELD MAPPING IN INGAN QUANTUM WELLS

The measurement of piezoelectric fields in quantum well structures is a challenging problem [71]. These fields which arise from changes in polarization e.g. at interfaces and can be partly screened by the accumulation of free carriers can lead to unwanted modifications of the band structure [72]. They can be reduced by various growth techniques which can reduce strain in the layers and thus the polarization. However, it is important to be able to make accurate measurements such that the effectiveness of these processing steps can be assessed. The polarisation fields are expected to be in the few MVcm^{-1} range and therefore sensitivity is less of an issue than for the measurement of fields in doped specimens. However, it is important to have high spatial resolution as the typical dimensions of these QW layers are just a few nm.

An $In_{0.15}GaN_{0.85}$/GaN superlattice with 6 quantum wells each of a nominal 2.2 nm thickness separated by 12 nm was examined in this study. Figure 11 shows an HR-STEM image that was acquired in order to assess the quality of the quantum wells. CBED patterns were also acquired and a specimen thickness of 106 $\pm$ 5 nm was measured. It is known that InGaN specimens can be sensitive to electron beam irradiation. Care was taken to align the

microscope on regions of the specimen that were not to be examined. However, even after prolonged irradiation of the specimen no major structural changes were detected.

For the DPC experiments, LM-DPC was not suitable as it could not provide the required spatial resolution. Therefore NB-DPC was used with an intermediate camera length of 1.2 m and a convergence angle of 2 mrads, again the acquisition time was 80 s to provide 1024^2 pixel maps. The specimen was tilted a few degrees from the [11-20] zone axis while taking care to not lose spatial resolution in projection. Figure 12 shows the effects of dynamical diffraction on the DPC imaging where (a)-(d) shows the different intensities measured on the individual detector segments A - D respectively and the sum of the segments is shown in Figure 12(e). Figures 12(f)-(i) show the intensities on the detector segments and (j) their sum when the specimen has been tilted from the previous orientation by a fraction of a mrad which is unmeasurable by the microscope goniometer. Now the contrast of the InGaN layers has changed and the reduction in dynamical scattering of the region of interests renders the data interpretable in terms of the electric field present.

The DPC intensities on the different detector segments were calibrated by manually displacing the transmitted beam using the method described earlier. Figure 13(a) shows an E_z map for the QW specimen acquired in NB-DPC mode using a camera length of 1.2 m and a convergence angle of 2 mrad and (b) shows the E_z profile acquired from the region indicated in (a). From only the convergence angle, a spatial resolution of about 0.8 nm can be estimated (not considering beam broadening in the specimen).

It is clear that there are large variations in the values of E_z in the different QWs. The values are shown in Table III and a variation between 2.2 and 3.5 $\pm$ 0.1 MVcm^{-1} has been measured. Figure 13(c) shows a E_z map also acquired in NB-DPC mode this time using a convergence angle of 4.2 mrads which leads to a probe size of around 0.4 nm. The effects of diffraction contrast in the two maps is evident and it becomes experimentally difficult to limit the diffraction as the convergence angle of the beam is increased. For the map acquired using a convergence angle of 2 mrads the background outside of the QW structures across the GaN region is flat, however for the map acquired using the convergence angle of 4.2 mrads, there is a large varying dark background on the signal arising from diffraction. The effects of diffraction are especially important for specimens such as these $In_{0.15}Ga_{0.85}N$ wells where bending of the lattice planes at the interfaces leads to varying diffraction conditions across the field of view. A related observation is that in the E_z maps in Figure 13(a) we observe

dark contrast at the top of each of the QWs and in (c) the dark contrast is at the bottom of the QWs. The difference in specimen orientation here between the two different maps is only a fraction of a mrad and as such great care must be taken during the interpretation of the data as diffraction can lead to important artefacts. The elimination of dynamical effects is difficult and large data series need to be acquired at different tilts such to provide a feeling of its impact on the measured fields. With increasing convergence angle it becomes more problematic to find tilt conditions (especially in the presence of sample bending) in which the diffraction disc intensity is homogeneous and free of dynamical contrasts over the region of interest, which is the assumption used in the data evaluation here of such a segmented detector setup.

The profile of the charge density, ρ can be obtained using

$$\nabla \cdot \mathbf{E} = \frac{\rho}{\varepsilon_0 \varepsilon_r}, \tag{18}$$

where ε_0 is the constant of permittivity and ε_r the relative permittivity. Figure 14(a) shows a charge density map and (b) profile calculated from the E_z map in Figure 13(c). The spatial resolution allows the interface dipoles at the top and bottom of the QW structure to be individually resolved. The charge measured at the bottom of the layers is systematically higher for the bottom interface than the top interfaces. This observation is qualitatively in agreement with simulations for this material system [73]. However, it is clear from Equation 18, that the presence of unwanted diffraction contrast will lead to strong artefacts in this measurement. Further discussion of this materials system is outside the scope of this article. For the DPC maps with lower convergence angle the fine structure of the charge accumulation (the sheet charges on both sides of each interface) were no longer resolved and are not shown here.

Electron holograms were also acquired of the specimen using Lorentz mode. Again the specimen was tilted to a weakly diffracting condition which was much more straightforward to achieve than for DPC as electron holography uses a very small convergence angle. However, the bending of the lattice planes at the QW interfaces can still lead to unwanted diffraction contrast and as such care must be taken to avoid this. An electron biprism voltage of 350 V was used to provide a fringe spacing of 0.8 nm which were reconstructed to provide phase images of the QW structure with a spatial resolution of 1.6 nm. However, when using the Lorentz lens the spatial resolution is limited by the aberrations of the imag-

ing system rather than by the fringe spacing, which is nominally 2.2 nm. It was not possible to obtain results with the required signal to noise from a single electron hologram. Therefore, as both good spatial resolution and sensitivity is required simultaneously, a stack of 32 electron holograms each of 8 s acquisition time was acquired using the Holoview software [27]. The registration of the stack is not straightforward as the beam, biprism and specimen will all independently drift during the acquisition. The sideband for each of the individual holograms was selected and an inverse Fourier transformation was applied to provide a stack of complex images which were aligned before the phase and amplitude components were reconstructed. This strategy allowed us to maintain a holographic fringe contrast of 16 % for a combined acquisition time of 256 seconds in order to maximise the signal to noise ratio.

Figure 15(a) shows an individual electron hologram of the QW structure, and (b) a detail of the hologram taken from the region indicated in (a) showing the fine interference fringes. The reconstructed amplitude image and potential maps are shown in 15(c) and (d) respectively. No unwanted diffraction contrast can be seen in the amplitude image which means that the measured phase can be directly interpreted. The improved signal to noise in the potential map means that FIB beam damage and contamination on the specimen surfaces is now clearly visible as bright spots. However, the potential map also has a much more homogenous contrast across the region of interest than observed for the DPC measurements. Figure 15(e) shows the extracted potential profiles and (f) the calculated values of E_z. The measured values of E_z values are shown in Table III and these are found to be in the range 3.30 to 3.82 $\pm$ 0.2 MVcm^{-1}.

The measured electric field by DPC and electron holography is also plotted as a function of the QW width in Figure 16 (widths were measured from the HAADF STEM images). For the electron holography measurements we observe that the electric field increases linearly with the well width. For the DPC measurements, there is also a linear fit although the measurements are not consistent with the holography. Inspection of the field maps in Figures 13(a) and 15(f) suggests that the DPC measurements are more strongly affected by diffraction, then the measured values of the fields could potentially be less accurate when compared to the holography due to the larger convergence angle.

IX. DISCUSSION

In this paper we have compared DPC and electron holography as techniques for measuring fields in different types of semiconductor devices. Electron holography can be used to provide phase images of the specimen from which the projected electrostatic potential can be calculated by knowing the thickness of the specimen. The signal to noise in the reconstructed phase images is related to the square root of the recorded electron counts and the interference fringe contrast. If high spatial resolution is required then finer holographic fringes are required which leads to a reduction in the field of view as the fringes need to be correctly sampled. In conventional single biprism holography the reference wave needs to pass through vacuum. In this work, when using fringe spacings of 0.8 nm to provide a spatial resolution of 1.6 nm, a field of view of 250 nm is achieved using a 2048 pixel detector so each fringe is sampled by 6 pixels. Therefore the region of interest needs to be around 250 nm from the surface. As such, additional specimen preparation steps or dedicated samples can be required for electron holography experiments in order to provide the vacuum reference. For large fields of view and less demanding spatial resolutions, fields of view of a micron can be achieved. One solution for the problem of having an adjacent reference wave to the region of interest is to use multiple biprisms [74], which is now common practice in laboratories that focus mainly on electron holography. As well as using optical setups to provide well sampled and fine interference fringes, the spatial resolution of electron holography can also be increased by using centre band suppression techniques such as phase shifting holography [75] and by using aberration correction in Lorentz mode [76].

DPC measures the local deflection of the transmitted beam in STEM mode which is related to the internal electric and magnetic fields. As shown here and elsewhere, the deflection can be related to the internal fields in and around a specimen. Quantification can be obtained by comparing the results to a known specimen that has been quantified using other techniques or by tilting the beam by a known value and measuring the intensities of the detector segments before and after. The accuracy of these quantifications is dependent on the stability of the microscope and descan and pivot point alignments which can be difficult to align for long camera lengths. The sensitivity of DPC measurements is in principal limited by the electrical and scan noise in the STEM imaging system. However, for most practical purposes the sensitivity can be improved by using a longer camera length to provide a large

measured shift of the transmitted beam.

The fixed size of the detector means that the convergence angle of the beam needs to be adjusted such that the beam diameter fits the detector geometry for a given camera length. As the convergence angle of the beam is related to the size of the electron probe in real space that can be formed, this also limits the spatial resolution. For example, for measurements of dopants which provide typical fields that are in the range 0.1 - 0.5 $MVcm^{-1}$, LM DPC could be used with camera lengths of about 10 m and convergence angles of 200 micro radians which would provide a spatial resolution of approximately 7 nm. For the measurements of piezoelectric fields which are typically above 1 $MVcm^{-1}$, a shorted camera length of 1.2 m could be used in NB-DPC mode which would require a convergence angle in the range 2 - 4 mrads and thus leads to a probe size below 1 nm. As discussed previously, the major problem for electron holography is the need for a reference wave which can be limiting for high spatial resolutions and is critical for atomic resolution. DPC does not require this reference and as such the fields can be measured using any magnification available. Another difference with DPC is that it can in principal be less prone to charging artefacts as the probe can be scanned across a desired area on the specimen avoiding regions containing insulating materials. When applying electron holography, a large area of the specimen is irradiated simultaneously and at a higher current and therefore charging can cause problems. This is especially the case for modern semiconductor devices such as SOI and FinFET technologies where small structures are typically surrounded by an insulating oxide region.

However, a detailed discussion of only the spatial resolution and sensitivity of the techniques would be misleading. The sensitivity can be increased by acquiring image stacks that are obtained using a low beam current. The sensitivity of both holography and DPC can also be improved by using better detectors. The most important discussion when comparing the techniques is the effects of dynamical diffraction. The effects of diffraction make the interpretation of reconstructed phase images or DPC field maps difficult. The key for making these types of measurements is to tilt the specimen to a weakly diffracting condition while limiting the projection problems of the region of interest and using the smallest possible convergence angle. In simple silicon specimens such as the p-n junction that was measured, this is relatively easy to achieve. However, for more complex materials such as the InGaN QW structures that were examined here, the situation is much more difficult. When using DPC, the small structure size necessitates a higher convergence angle which leads to more

artefacts from dynamical diffraction. For electron holography a (nearly) plane wave is used and as such weakly diffracting conditions can be found more easily and offer more robustness against sample tilts. For the measurements obtained by DPC, diffraction is a major problem and a compromise between spatial resolution and robustness of the measurement (and also between resolution and sensitivity) needs to be found for each type of specimen system. For these measurements of internal fields, thick specimens are typically required and as such dynamical diffraction is a problem that cannot be ignored.

In the last years fast pixelated detectors have been used for data acquisition in STEM and also for the case of electric field measurements [10, 80, 81]. It has been demonstrated that for measurements of atomic electric fields the center of mass needs to be determined using a camera to obtain quantitative values [34]. However, for samples thicker than a few nm even this approach fails. In contrast, electric fields in p-n junctions or piezo-electric fields of layers are homogeneous and do not vary over the beam intensity distribution leading to a simple shift of the diffraction disk without intensity redistribution within it [33]. The limitation is only the dynamical contrast that might change due to local sample tilts. This effect would does not only affect measurements with a segmented detector but also with a center of mass approach. A remedy could be to use precession [77–79] to suppress dynamical contrast in the diffraction pattern and/or to measure the beam displacement by means of template matching.

It is likely that segmented detectors will ultimately be replaced by the use of fast CCD cameras and the processing of giant data sets. An advantage of using a CCD camera is the flexibility to use different convergence angles which will lead to an improved spatial resolution when using long camera lengths. An additional advantage of course is to be able to use different processing techniques on the spatially resolved images of the transmitted beam to provide complementary information about the specimen.

X. CONCLUSIONS

In summary, electron holography and DPC have been assessed from the point of view of measuring the fields in real semiconductor devices. Although the sensitivity of the different methods can be increased by various means, electron holography seems to be more adapted for the measurement of low values of electrostatic fields whereas if dynamical diffraction can

be limited, DPC can provide a higher spatial resolution whilst maintaining a useful field of view. In general the different approaches each have their advantages and disadvantages and as such are complementary to each other. Both methods, if care is taken to avoid artefacts, can be powerful tools for semiconductor characterisation.

XI. ACKNOWLEDGEMENTS

These experiments have been performed using the Nanocharacterisation Platform at Minatec (PFNC). David Cooper thanks the European Research Council for the Starting Grant Stg:306535 "Holoview" for funding.

---

[1] A. Tonomura, Rev. Mod. Phys. **59**, 639-669 (1987)

[2] H. Lichte, P. Formanek, A. Lenk, M. Linck, C. Matzeck, M. Lehmann and P. Simon, Ann. Rev. Mat. **37**, 539 (2008)

[3] M.R. McCartney and D.J. Smith, Ann. Rev. Mat. **37**, 729 (2008)

[4] J.N. Chapman, P.E. Batson, E.M. Waddell and R.P. Ferrier, Ultramicroscopy, **3**, 203 (1978).

[5] J. Zweck J.N. Chapman, S. McVitie and H. Hoffmann, Magnetism and Magnetic Materials, **104**, 315 (1992).

[6] N. Shibata, S.D. Findlay, H. Sasaki, T. Matsumoto, H. Sawada, Y. Kohno, S. Otomo, R. Minato, Y. Ikuhara, Sci. Rep., **5**, 10040 (2015)

[7] T. Latychevskaia, P. Formanek, C.T. Koch and A. Lubk, Ultramicroscopy, **110**, 472 (2010)

[8] C.T. Koch and A. Lubk, Ultramicroscopy, **110** 460 (2010)

[9] C.T. Koch, Micron, **63** 69 (2014)

[10] M. W. Tate, P. Purohit, D. Chamberlain, K. X. Nguyen, R. M. Hovden, C. S. Chang, P. Deb, E.Turgut, J. T. Heron, D. G. Schlom, D. C. Ralph, G. D. Fuchs, K. S. Shanks, H. T. Philipp, D. A. Muller and S. M. Gruner., Microscopy and Microanalysis, **22**, 237 (2016)

[11] T.J. Pennycook, A.R. Lupini, H. Yang, M. Murfitt, L. Jones and P.D. Nellist, Ultramicroscopy, **151** 160 (2015)

[12] H. Yang, T.J. Pennycook and P.D. Nellist, Ultramicroscopy, **151** 232 (2015)

[13] P. A. Doyle and P. S. Turner, Acta Crystallogr., Sect. A, **24**, 390 (1968)

[14] D. Rez, P. Rez and I. Grant, Acta Crystallogr., Sect. A, **50**, 481 (1994)

[15] G. Radi, Acta Crystallogr., Sect. A, **26**, 41, (1970)

[16] Y.C. Wang, T.M. Chou M. Libera and T. F. Kelly, Appl. Phys. Lett. **70**, 1296 (1997)

[17] P. Kruse, M. Schowalter, D. Lamoen, A. Rosenauer and D. Gerthsen, Ultramicroscopy, **106**, 105 (2006).

[18] D. Cooper, J. Phys. D. **49** 474001 (2016)

[19] A. C. Twitchett, R. E. Dunin-Borkowski, and P. A. Midgley, Phys. Rev. Lett. **88**, 238302 (2002)

[20] A. Harscher and H. Lichte. Ultramicroscopy **64**, 57 (1994).

[21] H. Lichte, Ultramicroscopy **108**, 256 (2008).

[22] K. Yamamoto, I. Kawajiri, T. Tanji, M. Hibino and T. Hiriyama, J. Electron. Microsc. **49** 31 (2000)

[23] V. Boureau, Deformations introduites lors de la fabrication de transistors FDSOI : une contribution de l'holographiue electronique en champ sombre, Universitie de Toulouse 3 Paul Sabatier, (2016).

[24] D. Cooper, R. Truche, P. Rivallin, J. Hartmann, F. Laugier, F. Bertin and A. Chabli, App. Phys. Lett. **91** 143501 (2007).

[25] E. Voelkl and D. Tang, Ultramicroscopy, **110**, 447-459 (2010).

[26] R.A. McLeod, M. Bergen and M. Malec Ultramicroscopy **141**, 38 (2014).

[27] V. Boureau, B. Mayall, R.A. McLeod and D. Cooper Ultramicroscopy **194**, in press (2018).

[28] H. Rose, Optik, **39**, 416 (1974)

[29] H. Rose, Ultramicroscopy, **2**, 251 (1977)

[30] N.H. Dekkers and H. de Lang, Optik, **41**, 452 (1974).

[31] J.N. Chapman, Journal of Physics D: Applied Physics, **17**, 623 (1984).

[32] N. Shibata, Y. Kohno, S. Findlay, H. Sawada, Y. Kondo and Y. Ikuhara, J. Electron Microsc., **59** 473 (2010)

[33] K. Müller, F.F Krause, T. Grieb, S. Löffler, M. Schowalter, A. Beche, and J. Verbeeck, Ultramicroscopy, **178**, 62 (2017)

[34] K. Müller, F.F. Krause, A. Beche, M. Schowalter, V. Galioit, S. Löffler, J. Verbeeck, J. Zweck, P. Schattschneider and A. Rosenauer, Nat. Comms, **5**, 5653 (2014)

[35] R. Close, Z. Chen, N. Shibata, and S.D. Findlay, (2015). Ultramicroscopy, **159**, 124 (2014)

[36] N. Shibata, S.D. Findlay, Y. Kohno, H. Sawada, Y. Kondo, Y. Ikuhara, Nat. Phys., **8**, 611 (2012)

[37] M. Lohr, R. Schregle, M. Jetter, C. Wchter, T. Wunderer, F. Scholz, J. Zweck, Ultramicroscopy, **117**, 7 (2012)

[38] B. Bauer, J. Hubmann, M. Lohr, E. Reiger, D. Bougeard, J. Zweck, Appl. Phys. Lett., **104**, 211902 (2014).

[39] M. Lohr, R. Schregle, M. Jetter, C. Wächter, K. Mller, T. Mehrtens and J. Zweck, Physica Status Solidi (b), **253**, 140 (2016).

[40] L. Reimer, Scanning electron microscopy: physics of image formation and microanalysis (Vol. 45) Springer. (2013)

[41] D. Cooper, A.C. Twitchett, P.A. Midgley and R.E. Dunin-Borkowski, J. Appl. Phys. **101**, 094508 (2007).

[42] A.C. Twitchett, T. Yates, S.B. Newcomb, R.E. Dunin-Borkowski and P.A. Midgley, Nanoletters. **7** 2020 (2007).

[43] D. Cooper, A.C. Twitchett, P.A. Midgley and R.E. Dunin-Borkowski, J. Appl. Phys. **101** 094508 (2007).

[44] D. Cooper, C. Ailliot, J-P. Barnes, J-M. Hartmann, P. Salles, G. Benassayag and R.E. Dunin-Borkowski, Ultramicroscopy **110**, 383 (2010).

[45] M. Bellagia, P.F. Fazzini, P.G. Merli and G. Pozzi, Phys. Rev. B **67**, 045328 (2003).

[46] L. Houben, M.Luysberg and T.Brammer, Phys. Rev. B **70**, 165313 (2004).

[47] P.K.Somodi, A.C.Twitchett, P.A.Midgley, B.E.Kardynal, C.H.W.Barnes and R.E.Dunin-Borkowski,Ultramicroscopy **13**, 160 (2013).

[48] D. Cooper, C. Ailliot, R. Truche, J. Hartmann, J. Barnes, F. Bertin, J. Appl. Phys. **104**, 064513 (2008).

[49] D. Cooper, A.C. Twitchett, P.K. Somodi, I. Farrer, D.A. Ritchie, P.A. Midgley and R.E. Dunin-Borkowski, Appl. Phys. Lett. **88** 063510 (2006).

[50] Z. Wu, A.M. Fischer, F.A. Ponce, W Lee, J.H. Ryou, J. Limb and R.D. Dupuis. Appl. Phys. Lett., **91**, 041915 (2007)

[51] Z. Wu, M. Stevens, F.A. Ponce, W. Lee, J.H. Ryou, D. Yoo and R.D. Dupuis, Appl. Phys. Lett., **90**, 032101 (2007).

[52] F.A. Ponce. Annalen der Physik, **523**, 75 (2011)

[53] I. MacLaren, L. Wang, D. McGrouther, A. Craven, S. McVitie, R. Schierholz and R.E. Dunin-Borkowski, Ultramicroscopy, **154**, 57 (2015).

[54] P. Stadelmann, Ultramicroscopy, **131**, 21 (1987).

[55] D. Cooper, P. Rivallin, J-M. Hartmann, A. Chabli, R.E. Dunin-Borkowski, J. Appl. Phys. **106**, 064506 (2009)

[56] S.M. Sze and K.K. Ng, Physics of semiconductor devices. John Wiley and Sons. (2006)

[57] I. Lazic, E.G.T. Bosch and S. Lazar, Ultramicroscopy **160**, 265 (2016).

[58] W.D. Rau, P. Schwander, F.H. Baumann, W. Hoppner and A. Ourmazd, Phys. Rev. Lett. **82**, 2614 (1999).

[59] M.R. McCartney, M.A. Gribelyuk, J. Li, P. Ronsheim, J.S. Murray and D.J. Smith, Appl. Phys. Lett. **80**, 3213 (2002).

[60] M.A. Gribelyuk, M.R. McCartney, J. Li, S. Murthy, P. Ronsheim, B. Doris, J.S. McMurray, S. Hegde and D.J. Smith, Phys. Rev. Lett. **89**, 025052 (2002).

[61] M. A. Gribelyuk, V. Ontalus, F. H. Baumann, Z. Zhu, and J. R. Holt, J. Appl. Phys. **116**, 174501 (2004).

[62] M.G. Han, P. Fejes, Q. Xie, S. Bagchi, B. Taylor, J. Connor and M.R. McCartney, IEEE. Trans. Electron Dev. **54**, 3336 (2007).

[63] M.A. Gribelyuk, A. Domenicucci, P.A. Ronsheim, J.S. McMurray and O. Gluschenov, J. Vac. Sci. Tech. B **26**, 408 (2008).

[64] N. Ikarashi, M. Oshida, M. Miyamura, M. Saitoh, A. Mineji and S. Shishiguchi, Jap. J. App. Phys. **47** 2365 (2008).

[65] N. Ikarashi, A. Toda, K. Uejima, K. Yako, T. Yamamoto, M. Hane, and H. Sato, J. Vac. Sci. Technol. **B29**, 062201 (2010).

[66] M. A. Gribelyuk, Ph. Oldiges, P. A. Ronsheim, J. Yuan, and L. Kimball, J. Vac. Sci. Technol. **B29**, 062201 (2011).

[67] M. A. Gribelyuk, T. N. Adam, V. Ontalus, P. A. Ronsheim, L. Kimball and K. T. Schonenberg J. Appl. Phys. **110**, 063522 (2011).

[68] N. Ikarashi, H.Takeda, K.Yako, M.Hane, J. Appl. Phys. **100**, 143508 (2012).

[69] M. A. Gribelyuk, V. Ontalus, F.H. Baumann, Z. Zhu and J.R. Holt, Appl. Phys. Lett. **116**, 174501 (2014).

[70] D. Cooper, P. Rivallin, G. Guegan, C. Plantier, E. Robin, F. Guyot and I Constant, I. Semiconductor Science and Technology, **28**, 125013. (2013)

[71] Li, L., X. Hu and Y. Gao, Small. **14** 1701996 (2017)

[72] F. Bernardini, V. Fiorentini, and D.Vanderbilt. Phys. Rev. B **56**, 10024 (1997)

[73] K.Song, C.T. Koch, J.K. Lee, D.Y. Kim, J.K. Kim, A. Parvizi, W.Y. Jung, C.G. Park, H.J. Jeong, H.S. Kim, Y. Cao, T. Yang, L.Chen and S., **2** 1400281 (2012).

[74] K. Harada, A. Tonomura, Y. Togawa, T. Akashi and T. Matsuda, Appl. Phys. Lett., **84**, 3229 (2004).

[75] T. Tanigaki, S. Aizawa, H.S. Park, T. Matsuda, K.Harada, D. Shindo, Ultramicroscopy **137**, 7 (2014).

[76] S. McVitie, D. McGrouther, S. McFadzean, I. MacLaren, K.J. O'Shea and M.J. Benitez. Ultramicroscopy, 152, **57** (2015)

[77] R. Vincent and P. Midgley, Ultramicroscopy **53**, 271 (1994).

[78] J-L. Rouvière, A. Béché, Y. Martin, T. Denneulin and D. Cooper, App. Phys. Lett. **103**, 241913 (2013).

[79] D. Cooper, N. Bernier, J-L. Rouvière, Nano Lett. **15** 5289-5294 (2015).

[80] M. Krajnak, D. McGrouther, D. Maneuski, V. O'Shea, and S. McVitie, 165, **42** (2016)

[81] J.A. Mir, R. Clough, R. MacInnes, C. Gough, R. Plackett, I. Shipsey, I. MacLaren and V. O'Shea, Ultramicroscopy, **182**, 44-53 (2017)

FIGURES

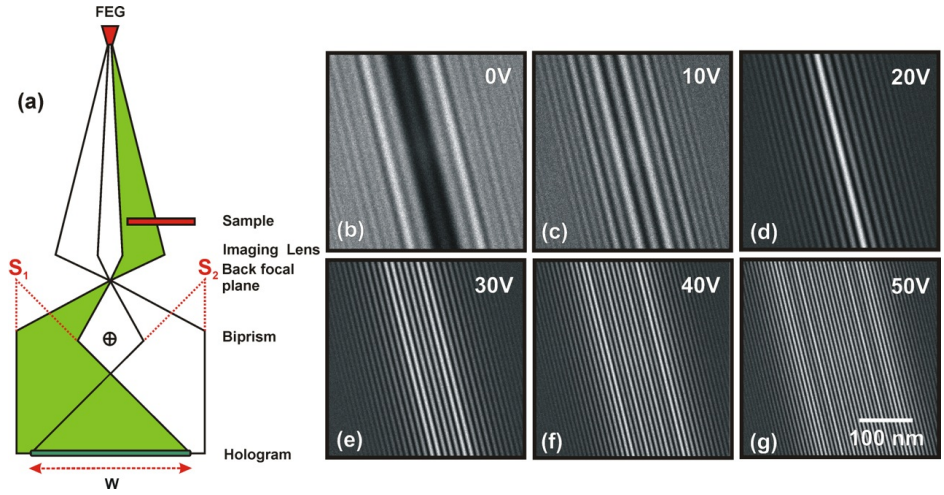

FIG. 1. (a) Schematic of the setup for off-axis electron holography. (b) Image of the biprism with no bias voltage applied. (c) -(g) Image of the electron interference fringes as the biprism voltage is increased from 10 - 50 V respectively.

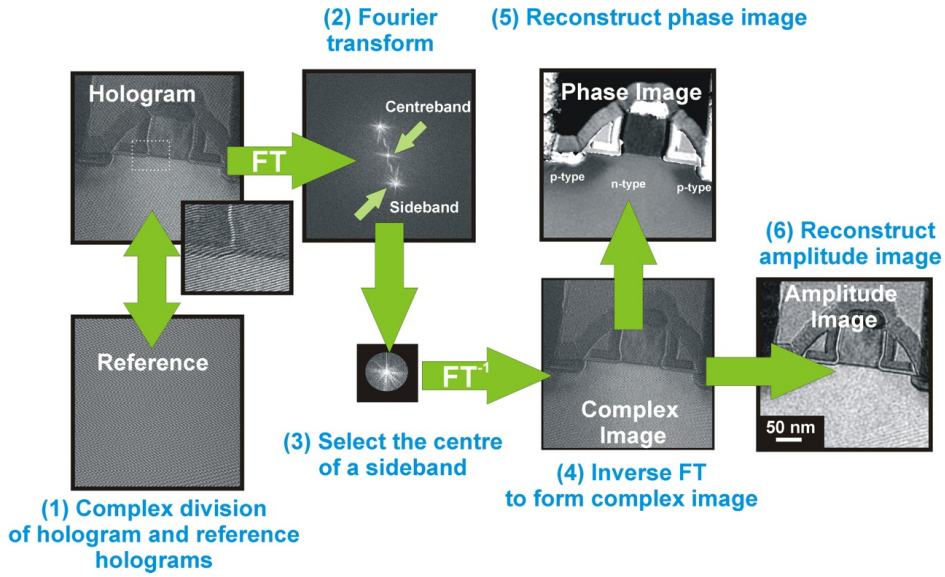

FIG. 2. The reconstruction procedure for off-axis electron holography

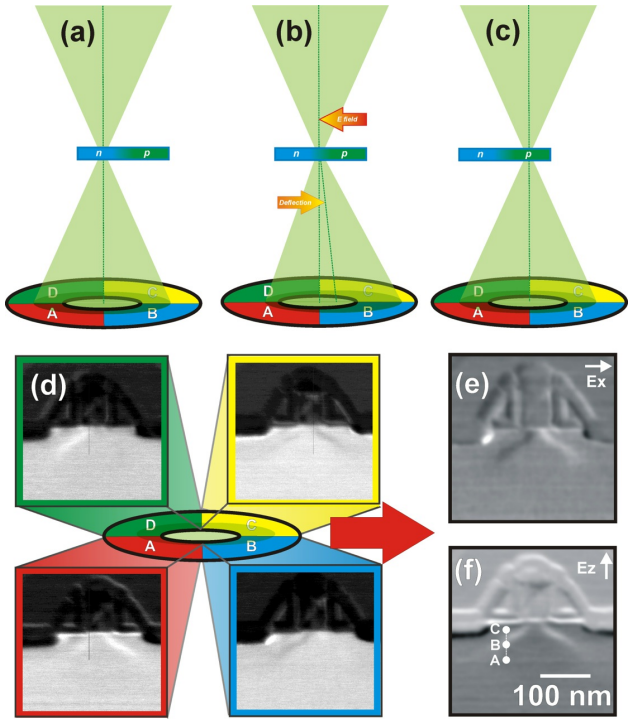

FIG. 3. Schematic showing the basic principal behind DPC. The convergent beam as it passes through a (a) p-type (b) depleted junction region and (c) n-type region. The beam is deflected by the electric field in the junction which leads to (d) different outputs for the different detector segments. By subtracting the segments from one another and then correcting for their rotation relative to the specimen, maps relating to the electric field in the (e) in-plane and (f) growth directions.

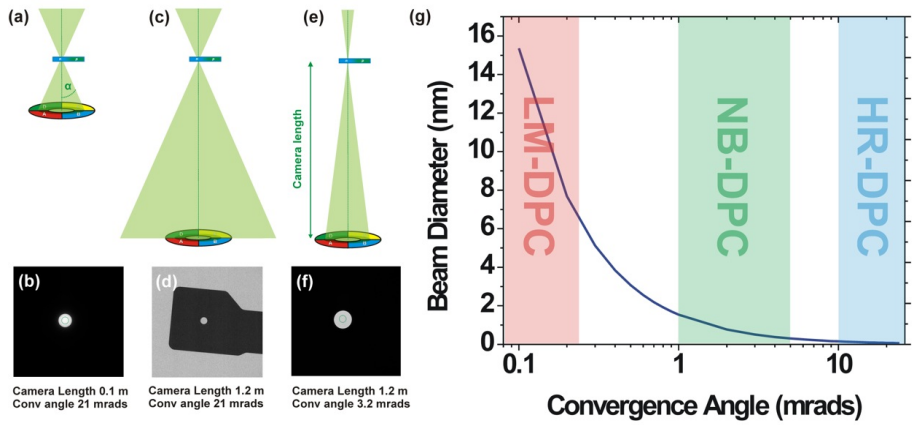

FIG. 4. (a) Schematic showing HR-DPC with a camera length of 0.15 m and beam convergence of 21 mrad incident on the segmented annular detector. (b) Image of the beam with the inner radius of the segmented annular detector indicated. (c) As the camera length is changed from 15 cm to 1.2 m to increase the sensitivity of the measurement (d) the beam becomes much larger than the detector. (e) Schematic of the NB-DPC optical arrangement with a camera length of 1.2 m and a convergent beam of 3.2 mrad (f) such that the beam diameter is again roughly twice the inner radius of the annular detector. (g) Plot of diffraction limited beam diameter as a function of convergence angle, neglecting the influence of source size and aberrations. The approximate working parameters for HR, NB and LM-STEM are indicated.

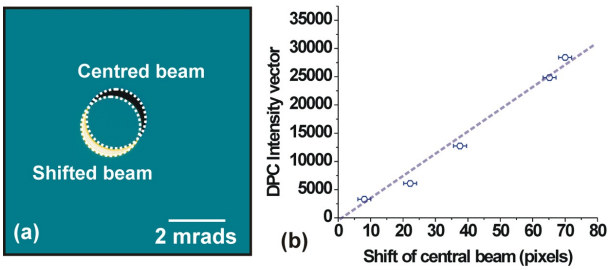

FIG. 5. (a) Image showing initial position of beam and shifted beam. (b) The magnitude of the beam shift vector measured on the camera as a function of the absolute value of the intensity difference vector measured by the segmented annular detector.

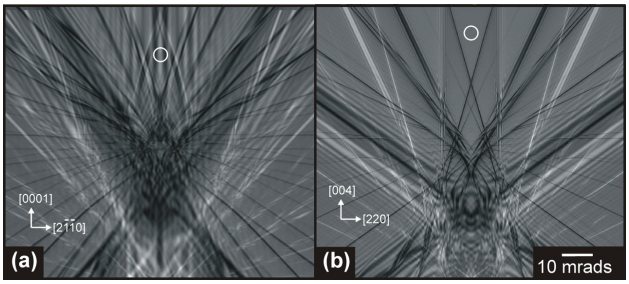

FIG. 6. Simulated CBED patterns for 200 kV electron beam incident on (a) 100 nm-thick GaN specimen and (b) a 300-nm-thick Si specimen tilted 1.5 degrees from the zone axis along the [0001] and [004] directions respectively. The indicated circles have a diameter of 4 mrads.

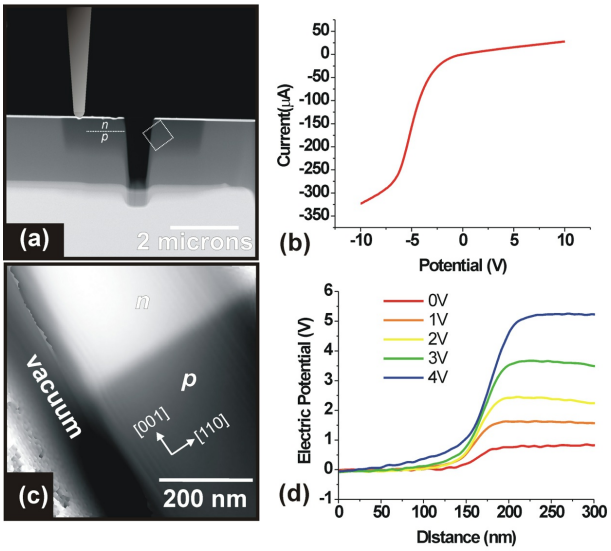

FIG. 7. (a) STEM image of the diode that was examined in situ. (b) Current / Voltage characteristics of the diode after preparation. (c) Phase image of the diode acquired using off-axis electron holography at a reverse bias of 4.0 V. (d) The measured potential across the diode for different reverse bias voltages.

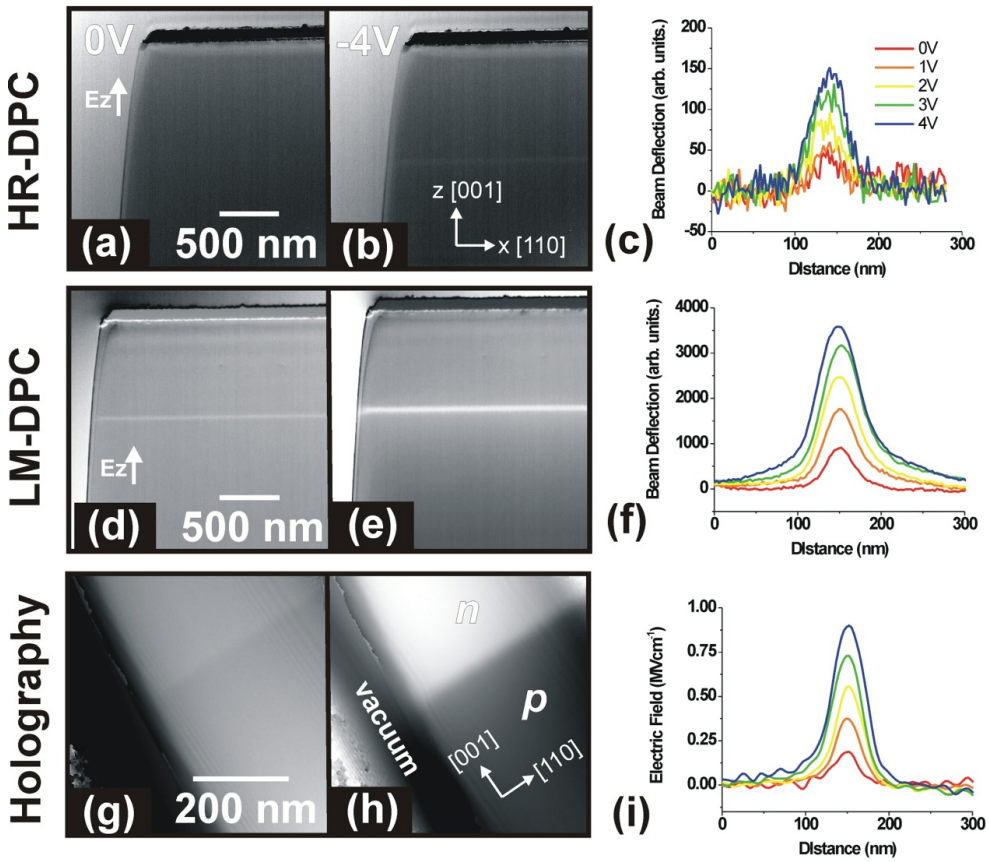

FIG. 8. (a) E_z map at 0V and (b) 4V reverse bias and (c) E_z profiles acquired using HR-DPC at different reverse bias voltages. (d) E_z map at 0V and (e) 4V reverse bias and (f) electric field profiles acquired using LM-DPC at different reverse bias voltages. (g) Potential map at 0V and (h) 4V reverse bias and (i) E_z profiles calculated from the potential profiles acquired using electron holography for different reverse bias voltages.

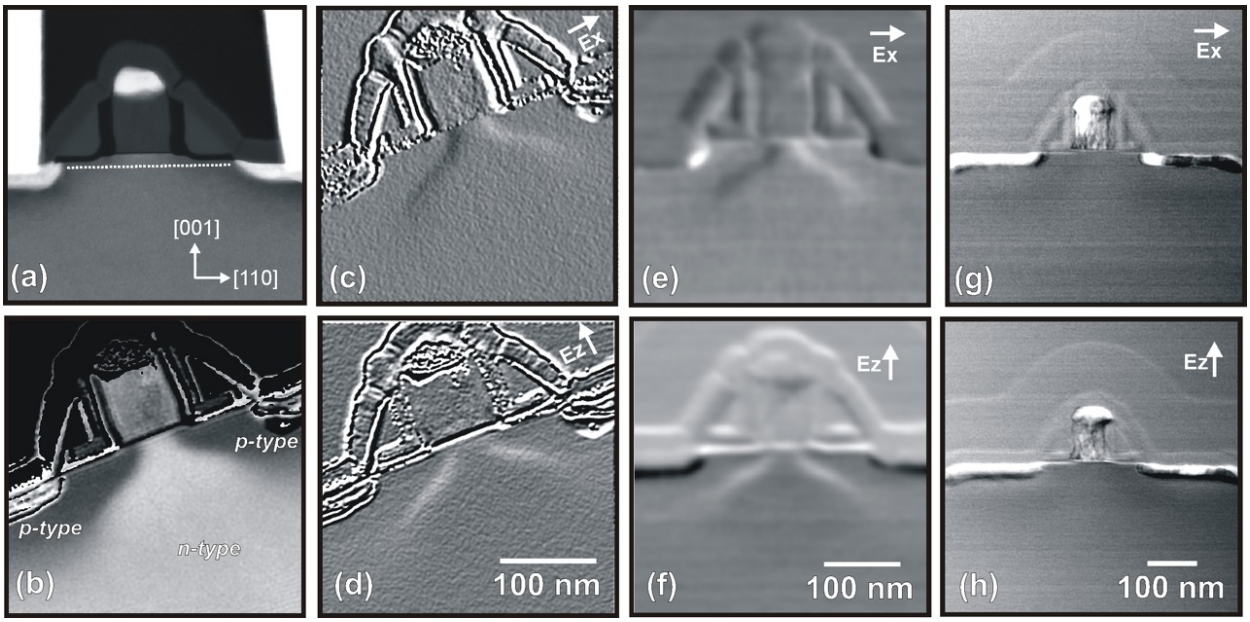

FIG. 9. (a) HRSTEM image of a silicon p-MOS device. (b) Potential map acquired by electron holography. (c) E_x map calculated from the electrostatic potential map in (b). (d) E_z map calculated from the potential map shown in (b). (e) E_x map acquired by LM-DPC. (f) E_z map acquired by LM-DPC. (g) E_x map acquired by HR-DPC. (h) E_z map acquired by HR-DPC.

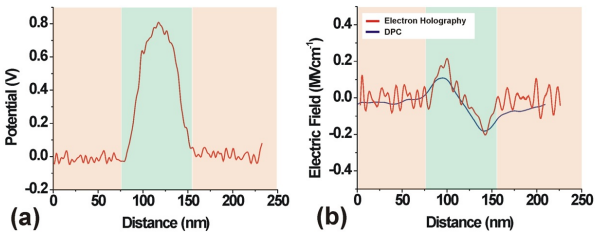

FIG. 10. (a) Potential profile obtained by electron holography and (b) E_x profile acquired from across the region indicated in 9(a) for the field maps acquired by electron holography and DPC.

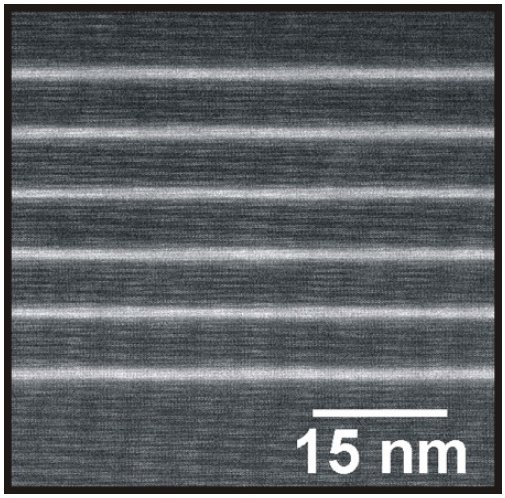

FIG. 11. (a) HAADF STEM image of a series of 2.2-nm-wide $In_{0.15}Ga_{0.85}N$ quantum wells in GaN.

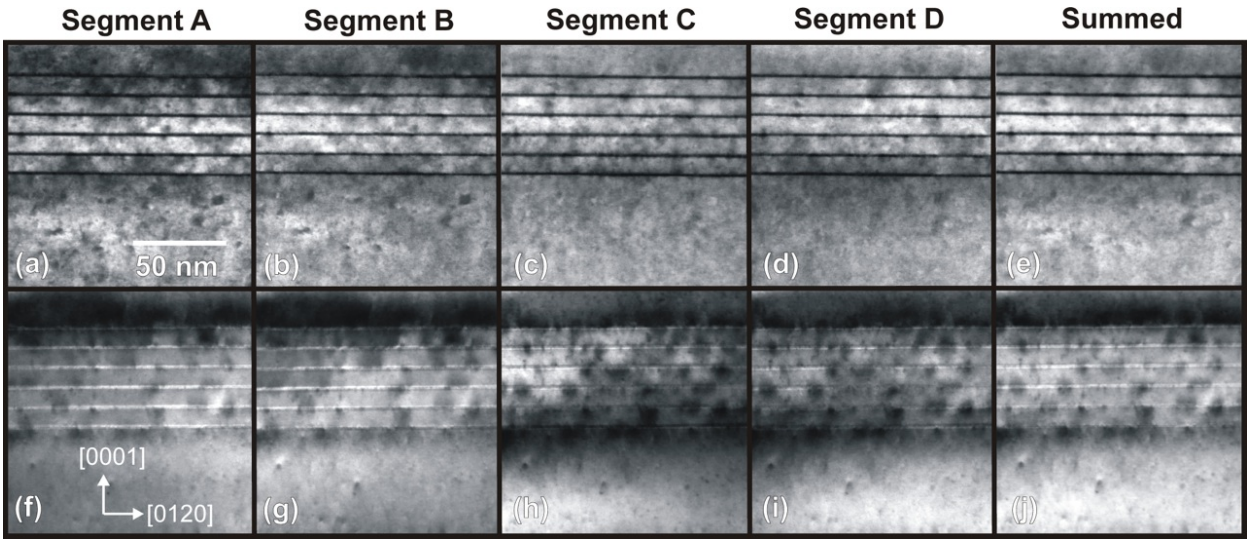

FIG. 12. (a) - (d) Intensity measured on the different DPC detector segments A - D respectively and (e) their sum with the specimen in a at an orientation not suitable for DPC analysis. (f) - (i) Intensity measured on the different DPC detector segments A - D and (j) their sum with the specimen in an appropriate orientation for DPC analysis.

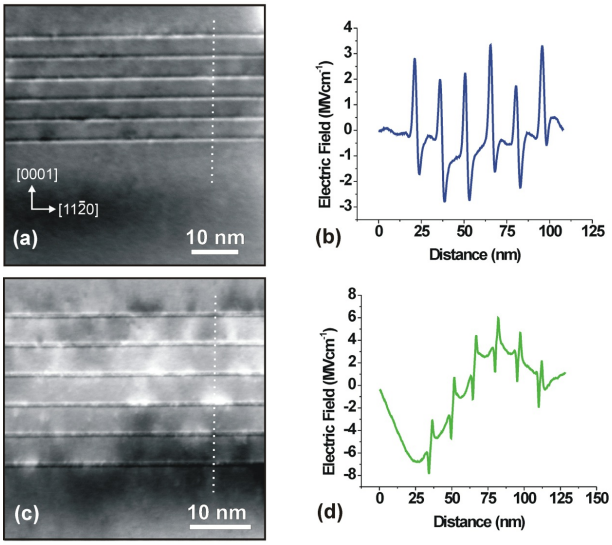

FIG. 13. (a) Electric field map for a series of 2.2-nm-wide $In_{0.15}Ga_{0.85}N$ quantum wells in GaN acquired by HR DPC using a camera length of 1.2 m and a convergence angle of 2 mrad. (b) Electric field profile acquired from the region indicated in (a). (c) Electric field map for the same sample acquired by HR DPC using a camera length of 1.2 m and a convergence angle of 4.2 mrad. (d) Electric field profile acquired from the region indicated in (c).

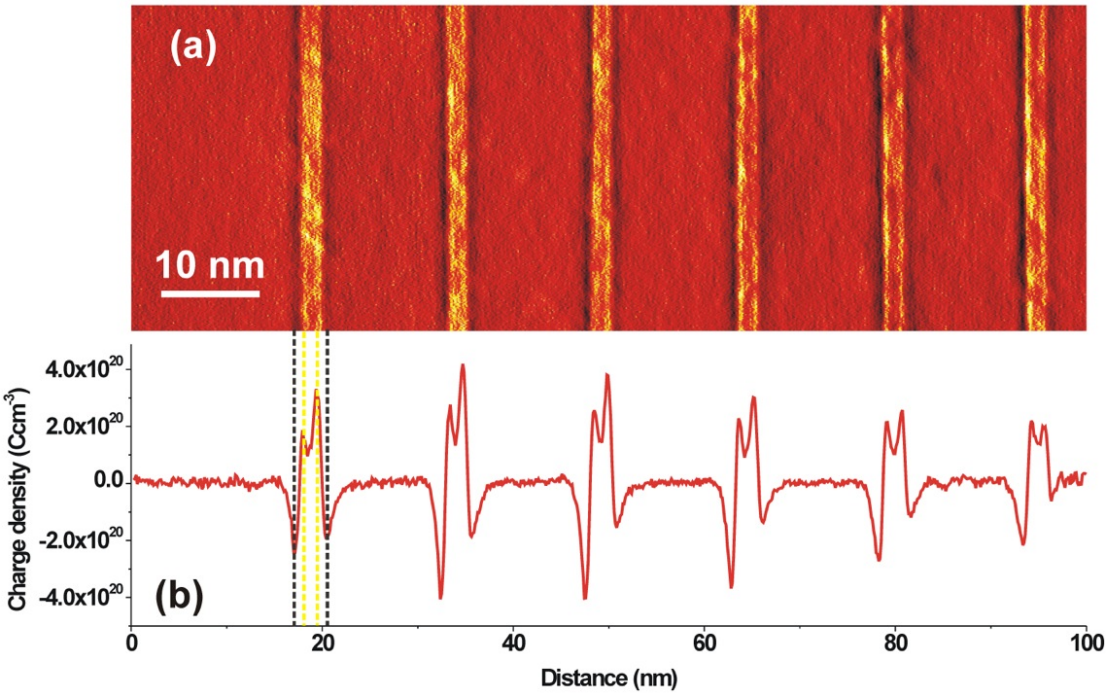

FIG. 14. (a) Charge density map for a series of 2.2-nm-wide $In_{0.15}Ga_{0.85}N$ quantum wells in GaN acquired by NB-DPC using a camera length of 1.2 m and a convergence angle of 4.2 mrads. (b) Charge density profile acquired from the region indicated in (a) corresponding quantitatively well for predictions for this system [73]

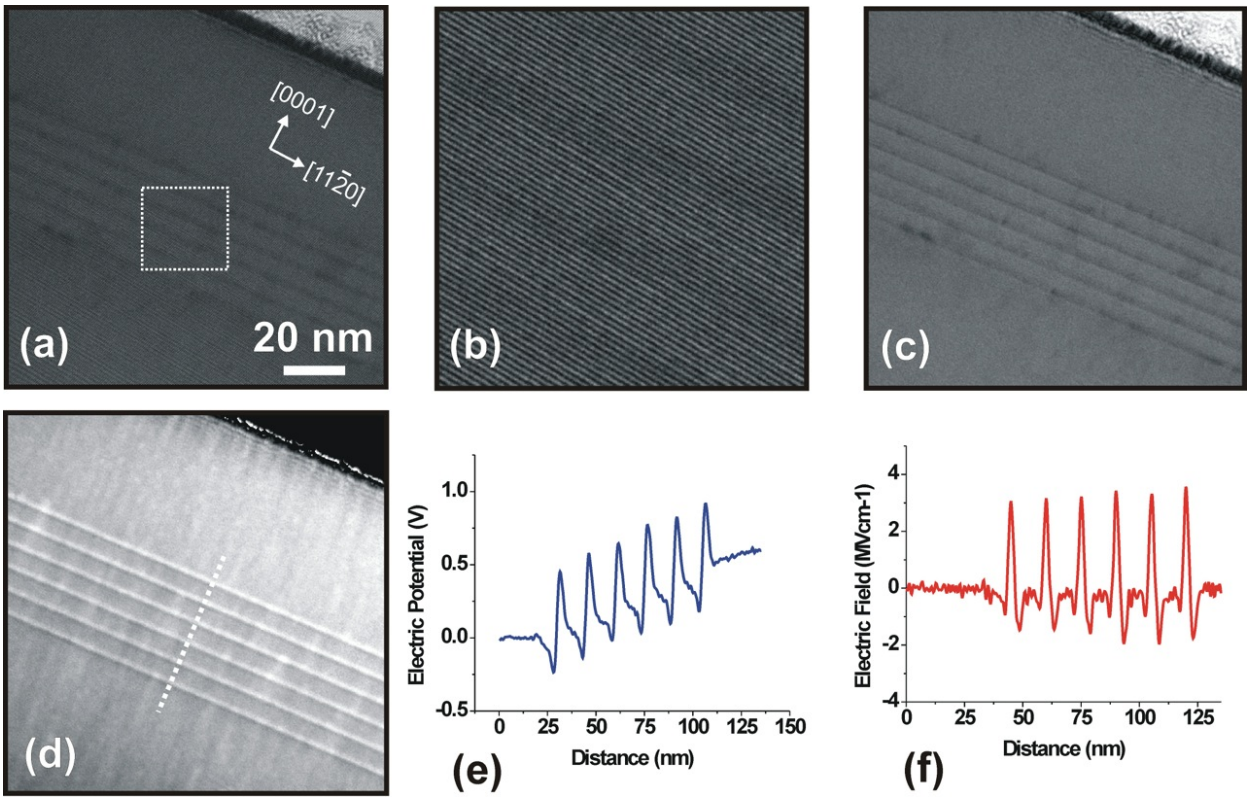

FIG. 15. (a) Electron hologram of the QW structure. (b) Detail from indicated region in (a). (c) Reconstructed amplitude image showing the absence of diffraction contrast. (d) Potential map of the QWs calculated from the reconstructed phase images. (e) Potential profiles for the QWs taken from the profile shown in (b) and averaged across 50 nm. The gradient on the potential comes from doping in the device. (f) Calculated electric field for the QWs.

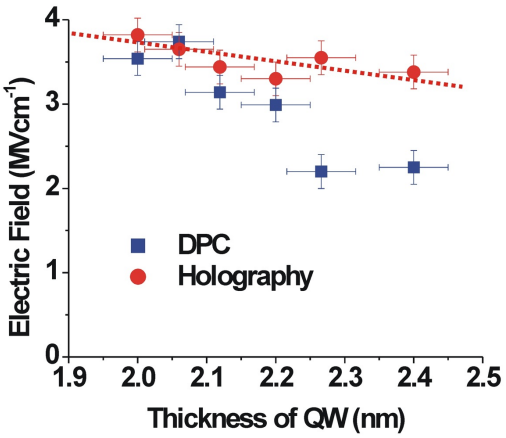

FIG. 16. Measured electric field by electron holography and DPC as a function of QW width.

TABLES

Mode	Convergence angle	Probe size	Camera length	Sensitivity	Application
HR-DPC	20 mrad	< 0.1 nm	0.1 m	Low	Atomic E-fields [34, 36]
NB-DPC	2 mrad	1 nm	1 m	Moderate	Piezo-electric fields [39]
LM-DPC	0.2 mrad	10 nm	10 m	High	E-field in p-n junction [6]

TABLE I. Comparison of typical convergence angles, resulting probe size, camera length, sensitivity and application for the three DPC modes high-resolution (HR), nano-beam (NB) and low-magnification (LM).

Technique	**HR-DPC**	**LM-DPC**	**Electron Holography**
Resolution	< 0.1 nm	7.5 nm	7.5 nm
FOV	2.5x2.5 μm^2	2.9x2.9 μm^2	1.6x0.6 μm^2
SNR	0.6	45	55 (470 for phase)
Frame time	80 s	80 s	8 s

TABLE II. Comparison of HR-DPC and LM-DPC vs. off-axis holography for the performed experiments. The signal to noise is assessed by dividing the total signal by the RMS noise at a reverse bias of 4 V.

Technique	Well 1	Well 2	Well 3	Well 4	Well 5	Well 6
HAADF STEM thickness (nm)	2.26	2.41	2.20	2.26	2.11	2.09
NB-DPC field at 2 mrads ($MVcm^{-1}$)	2.99	2.25	3.14	3.74	2.20	3.54
Holography field ($MVcm^{-1}$)	3.30	3.38	3.44	3.65	3.55	3.82

TABLE III. Measured properties of the QW layers with Well 1 referring to the bottom. Errors are ± 0.05 nm for the STEM thickness measurement and $\pm$ 0.2 $MVcm^{-1}$ for the holography measurements of fields.